Available online at www.sciencedirect.com
ScienceDirect
Geochimica et Cosmochimica Acta 73 (2009) 6098–6113
Geochimica et Cosmochimica Acta
www.elsevier.com/locate/gca

Dissolution of olivine during natural weathering

Michael A. Velbel *

Department of Geological Sciences, 206 Natural Science Building, Michigan State University, East Lansing, MI 48824-1115, USA

Received 16 September 2008; accepted in revised form 22 July 2009; available online 28 July 2009

Abstract

Naturally weathered olivine occurring as phenocrysts in Hawai'ian volcanic rocks from several volcanic centers and regolith/outcrop settings, and as tectonized olivines from several metadunite bodies in the southern Appalachian Blue Ridge, are all similarly corroded by natural weathering. Conical (funnel-shaped) etch pits occur as individual pits, base-to-base pairs of cone-shaped pits, or *en echelon* arrays. Etch-pit shapes and orientations in the smallest etch-pit arrays visible in conventional scanning electron microscopy resemble even smaller features previously reported from transmission electron microscope investigations of olivine weathering. Etch pits occur in samples with chemical and/or mineralogical evidence of weathering, and/or are associated with, or proximal or directly connected to, fractures or exposed outcrop surface, and therefore are formed by weathering and not inherited from pre-weathering aqueous alteration (e.g., serpentinization, iddingsitization) of these parent rocks. Many etch pits are devoid of weathering products. Natural weathering of olivine is surface-reaction-limited. Similarity of corrosion forms from naturally weathered olivine from multiple igneous and metamorphic parent-rock bodies suggests that olivine weathers in the same manner regardless of its specific crystallization/recrystallization history, eruption/weathering/exposure ages of the olivine's host rock, and the local regolith history.

1. INTRODUCTION

The purpose of this paper is to describe mineral-surface textures formed by aqueous corrosion during natural weathering of olivine. Textural studies are essential to understanding low-temperature mineral–water interactions, especially their reaction kinetics, which are usually slow enough to prevent mineral–solution systems from reaching thermodynamic equilibrium (e.g., Lasaga, 1998). There are four tests to determine whether the rate-determining process in mineral–water interactions is reaction at the mineral–environment interface or diffusion of reactants and/or products to/from the primary mineral interface through the surrounding medium (Berner, 1978). However, three of these tests apply exclusively to experimental systems or natural systems in which the solution still co-exists with the reacting mineral and is available for chemical analysis of solutes (Berner, 1978). Only one (textural) test can be applied to naturally altered materials lacking presently co-existing solutions (Velbel, 2004).

Overviews of observations from naturally weathered mineral grains and implications for reaction mechanisms have been published for rock-forming silicates as a whole (Wilson, 1975, 2004; Velbel, 1993), for other specific major silicate mineral groups (e.g., feldspars – Berner and Holdren, 1977, 1979; Velbel, 1986; Lee and Parsons, 1995; Lee et al., 1998, 2007; Parsons et al., 2005; Brown and Lee, 2007: chain-silicates – Berner et al., 1980; Berner and Schott, 1982; Velbel, 2007), and even for some less-common rock-forming silicates (e.g., garnets – Velbel, 1984; Velbel et al., 2007; staurolite – Velbel et al., 1996; epidote-group minerals – Price et al., 2005) but a similar synthesis for olivine is lacking. This paper fills that gap.

Varieties of low-temperature aqueous alteration other than corrosion (e.g., olivine replacement by clays) and higher-temperature aqueous alteration (e.g., serpentinization of olivine) have been reviewed elsewhere (Wicks and Whittaker, 1977; Delvigne et al., 1979; Wilson, 2004) and are discussed in this paper only where required in relation to corrosion. Similarly, this paper does not systematically

* Tel.: +1 517 353 5273; fax: +1 517 353 8787.
E-mail address: velbel@msu.edu

0016-7037/$ - see front matter © 2009 Elsevier Ltd. All rights reserved.
doi:10.1016/j.gca.2009.07.024

review the literature on experimental dissolution kinetics of olivine, but discusses those experimental papers that reported surface textures.

In order to provide a uniform basis of comparison of samples from multiple parent-rock types and study areas, this paper emphasizes corrosion features formed by natural weathering and visible by two widely available methods, optical petrography and (primarily) scanning electron microscopy (SEM) in both secondary and backscattered electron imaging modes (SEI and BEI, respectively). Comparison is made with relevant published observations made using other methods where applicable.

1.1. Background and previous work

Olivine weathers more rapidly than any other major rock-forming silicate mineral (Goldich, 1938; Wilson, 2004) or other common orthosilicate (Velbel, 1999), so olivine does not usually survive to be part of the heavy-mineral fraction of most soils, sediments, or sedimentary rocks (Delvigne et al., 1979; Morton and Hallsworth, 1999; Wilson, 2004). Consequently, there are very few studies of olivine alteration textures in the literature on weathering or sedimentary petrology. Hay (1959) reported (without illustration) from optical petrographic study that fayalitic olivine is more extensively weathered than magnesian (forsteritic) olivine in naturally weathered volcanic breccia and tephra. The outstanding petrographic studies of olivine replacement textures and products by Wilshire (1958) and Delvigne et al. (1979) predate the application of scanning electron microscopy to mineral surfaces, and thus shed little light on the topics of this paper. Likewise, there is an extensive literature on the natural alteration of olivine to iddingsite and/or other phyllosilicate products of weathering and other aqueous alteration (e.g., Delvigne et al., 1979; Eggleton, 1984; Smith et al., 1987; Delvigne, 1998), but little of this literature describes olivine surface textures beneath the secondary minerals. Nahon et al. (1982a) presented SEM images of striated but unaltered forsterite, and a mass of ferruginous alteration product completely replacing forsterite, but no etching or corrosion features.

Wilson and Jones (1983) observed deep etching in olivine from soil on weathered gabbro; Wilson (2004) reviewed the earlier results and presented additional SEM imagery from the same study area. Smith et al. (1987) used SEM to illustrate a cross-section through an olivine–iddingsite interface, secondary minerals precipitated on an apparently unaltered olivine surface, and a mass of olivine completely replaced by iddingsite, but no etching or corrosion features. Optical petrographic and SEM reconnaissance of weathered basalt near Schofield Barracks, Oahu (locality described by Patino et al. (2003)) revealed chains of elongate, elliptical, or almond-shaped etch pits (with pointed rather than rounded ends in some cross-sections) aligned laterally along the shortest axis of the pits; an SEM image of one such etch-pit chain from olivine at this locality was presented by Velbel (1993). Velbel and Ranck (2008) examined naturally weathered olivine from several metamorphosed, tectonized metadunite bodies and found funnel-shaped etch pits. Large etch pits are associated with macroscopic weathering features (weathering rinds) and therefore form by weathering, and are not inherited from pre-weathering alteration of these rocks (Velbel and Ranck, 2008). However, it remains unclear whether the presence of small etch pits in the portions of metadunite samples lacking macroscopic weathering features indicates that some olivine corrosion is produced by pre-weathering aqueous alteration (e.g., serpentinization), or that small amounts of localized weathering have already affected such otherwise-fresh samples (Velbel and Ranck, 2008). Several papers predominantly or exclusively about transmission electron microscopy of olivine alteration to secondary minerals (e.g., Eggleton, 1984, 1986; Smith et al., 1987; Banfield et al., 1990) also contain information relevant to the interpretation of larger-scale alteration phenomena visible in SEM.

Where olivines of more than one composition occur and weather in the same material (e.g., fragmental rocks such as volcanic breccias and tephra), the more fayalitic (ferriferous) olivine is weathered to a greater extent than is more forsteritic (magnesian) olivine (e.g., Hay, 1959). The results of laboratory dissolution-kinetics experiments (Wogelius and Walther, 1992) and considerations of crystal-chemistry and bond strengths (Schott and Berner, 1985; Velbel, 1999) are consistent with this observation.

2. MATERIALS AND METHODS

2.1. Samples

Olivine-bearing samples examined for this study come from multiple field areas on each of two parent-rock types; olivine-phyric basalt, and metadunite. Information on the field area, parent-rock type, regolith and exposure types, sample type, and (where known or retrievable) olivine composition and major-element weathering indices for each sample or sample suite is summarized in Table 1.

2.1.1. Basalt

Samples from two localities on volcanic rocks (one locality each from two Hawai'ian islands) were examined for this study. The work on the Hawai'ian-island samples reported here examines the same collection of polished thin sections from young lava flows from which Cochran and Berner (1996) and Berner and Cochran (1998) selected their published images. Samples from lava-flow surfaces represent the initial response of volcanic rock and minerals to weathering upon exposure of fresh rock directly at the land surface without development of any regolith.

The petrographic work reported here from Schofield Barracks, Oahu, is on the two least-weathered spheroidally weathered (Ollier, 1967, 1971) vesicular subalkaline basalt samples Patino et al. (2003) analyzed for bulk chemistry. Olivine phenocrysts were examined from a slightly weathered corestone (HS-1) and an exfoliated shell approximately one meter from the corestone center (HS-2). The shell has experienced more chemical weathering than the core, as illustrated by differences in several chemical weathering indices between the core and the shell.

Common major-element weathering indices use abundances of alkalis and alkaline earth elements in weathering products of silicate rocks to quantify differences in overall chemical weathering among suites of related samples. In applying indices involving Ca to silicate weathering, bulk CaO is corrected by subtracting the portion of CaO in the bulk analysis that is associated with carbonates or phosphates; the corrected lime abundance is indicated as CaO^*. Some major-element indices quantify weathering by loss of mobile elements relative to a less-mobile element (e.g., Al).

Table 1
Sample locality attributes, olivine compositions, and information sources.

Sample suite	Field locality	Rock type	Regolith type	Exposure	Sample type	Fo	Fa	CIA[a]	WIP[b]	Reference(s)[c]
Flow	Hawai'i	Basalt	Constructional	Lava-flow surface	Flow surface	68–78	22–32	n/a	n/a	Cochran and Berner (1996) and Berner and Cochran (1998)
Schofield Barracks	Oahu	Basalt	Residual/relict	Roadcut	Corestone	83–85	15–17	66	61	Patino et al. (2003)
Schofield Barracks	Oahu	Basalt	Residual/relict	Roadcut	Exfoliated shell around corestone	84–87	13–16	92	46	Patino et al. (2003)
Day Book complex	Burnsville, NC	Dunite	Residual/relict	Roadcut	Weathered rind	91–93	7–9	n/a	n/a	Carpenter and Phyfer (1975)
Webster–Addie complex	Sylva, NC	Dunite	Residual/relict	Roadcut	Weathered rind	92–94	6–8	n/a	n/a	Miller (1953)
						90.6–91.0	9.0–9.4			EDS (this study)
Laurel Creek complex	Northeast GA	Dunite	Residual/relict	Roadcut	Weathered rind	80–94	6–20	n/a	n/a	Feiss et al. (1991)

n/a indicates bulk composition unavailable for determination of weathering indices, or rock type unsuitable for common major-element weathering indices.
[a] CIA = Chemical Index of Alteration (see text).
[b] WIP = Weathering Index of Parker (see text).
[c] Source for description of field area, parent-rock unit, sample, and/or olivine composition.

The Chemical Index of Alteration (CIA; applied to volcanic rocks by Nesbitt and Wilson, 1992) uses measured values of potash, soda and lime (CaO^*) from silicate weathering. Under most weathering conditions, the cations of these oxides are mobile relative to alumina, the oxide of the least mobile major element. Using these choices of weathering-mobile and weathering-immobile elements,

$$CIA = (100)[Al_2O_3/(Al_2O_3 + CaO* + Na_2O + K_2O)]$$

CIA increases with increased chemical weathering (Nesbitt and Wilson, 1992; Price and Velbel, 2003). CIA for the slightly weathered Oahu corestone is 66, whereas CIA is 92 for the moderately weathered shell (calculated from the data of Patino et al., 2003), indicating more extensive loss of alkalis and alkaline earths from the shell than the corestone.

Table 1 also shows the Weathering Index of Parker (WIP; also known as the Parker Index) which is based on abundances of alkalis and alkaline earth elements in weathering products of silicate rocks (Parker, 1970);

$$WIP = (100)[(2Na_2O/0.35) + (MgO/0.9) + (2K_2O/0.25) + (CaO*/0.7)]$$

These elements are the most mobile of the major elements, and the WIP also takes into account the differential individual mobilities of Na, K, Mg, and Ca, based on their bond strengths with oxygen (Parker, 1970). WIP decreases with increased chemical weathering (Price and Velbel, 2003). WIP for the slightly weathered Oahu corestone is 61, whereas WIP is 46 for the moderately weathered shell (calculated from the data of Patino et al., 2003), indicating more extensive loss of alkalis and alkaline earths from the shell than the corestone.

Both commonly used major-element-based weathering indices, CIA and WIP, show the Schofield Barracks shell sample to be more weathered than the corestone, even though both samples show similar REE indications of weathering (Patino et al., 2003). The Schofield Barracks suite emphasizes moderately weathered early to intermediate stages of volcanic rock- and mineral-weathering in a regolith/outcrop setting that is extensively weathered overall.

2.1.2. Dunite

Metamorphosed olivine-rich peridotites and dunites are numerous and widespread in the southern Appalachian Blue Ridge, and include some bodies not extensively modified by hydrous alteration of olivine to hydrated minerals (Hatcher et al., 1984; Feiss et al., 1991). Bedrock in the region consists predominantly of high-rank (amphibolite facies) metasedimentary schists and gneisses, with local pods of tectonized mafic–ultramafic lithologies (Hatcher et al., 1984, 2005; Swanson et al., 2005). Olivine in southern Blue Ridge ultramafic rocks ranges in composition from $Fo_{80–94}$ (Feiss et al., 1991). Most mafic/ultramafic units were strongly deformed and recrystallized during regional metamorphism (McSween and Hatcher, 1985; Ryan et al., 2005; Swanson et al., 2005). Meshwork serpentinization (Wicks and Whittaker, 1977) of olivine is a minor but nearly ubiquitous feature of olivine in many metadunite bodies; serpentinization is retrograde metamorphic and occurred after peak metamorphic conditions formed a variety of metamorphic minerals including one or more amphiboles, chlorite, talc and vermiculite (Ryan et al., 2005; Swanson et al., 2005). Visibly oxidized weathered rinds on dunite corestones from three partially serpentinized metamorphosed ultramafic bodies in the southern Appalachian Blue Ridge (the Day Book, Webster–Addie and Laurel Creek complexes) were examined for this study. Common major-element weathering indices cannot be used to characterize the degree of weathering of ultramafic rocks, since most weathering indices include alkalis (as mobile elements) and alumina (as an ''immobile" element), which are present as only minor and usually variable and heterogeneously distributed constituents of ultramafic rocks.

2.2. Sample preparation and analysis

All samples were examined by optical petrography and scanning electron microscopy (SEM), except the sample from the Day Book ultramafic body (SEM only). The weathered Day Book sample was ultrasonically cleaned to remove alteration products and fine particulate dust; to minimize possible sample preparation artifacts all other samples were mounted without any additional treatment to remove weathering products or dust. Small chips of air-dried partially weathered rock were glued to aluminum stubs, coated with Au, and examined in secondary electron imaging (SEI) mode using one of the following SEMs; an ETEC Corporation Autoscan U-1 SEM with a Polaroid camera at the Yale Peabody Museum (Day Book; Schofield Barracks, Oahu), a JEOL T-20 SEM with a Polaroid camera in the Department of Geological Sciences at Michigan State University (Webster–Addie) and a JEOL 6400 SEM equipped with digital image acquisition and Noran and Oxford energy dispersive spectroscopy (EDS) systems at the Center for Advanced Microscopy at Michigan State University (Schofield Barracks, Webster–Addie). All SEMs used for this study are conventional (Wo filament or LaB_6 emitter) SEMs, with point-to-point spatial resolutions of ~20 nm.

Polished uncovered thin sections of the samples from the islands of Oahu and Hawai'i, and from the Webster–Addie and Laurel Creek complexes from the southern Blue Ridge, were examined in both SEI and backscattered electron imaging (BEI) mode on the same JEOL 6400 SEM/EDS systems described in the previous paragraph.

In SEI, contrast is due mainly to topographic variations on the grain or chip surface; SEI is used to examine the three-dimensional geometry of corrosion features on grain surfaces. In backscattered electron imaging (BEI) mode, contrast is due mainly to spatial variations in atomic number (Z); BEI is used to examine two-dimensional slices through grains, and gives insight into the penetration of corrosion features into grain interiors. Since both the reactant and product minerals in this study are silicates and oxides of major rock-forming elements, the element primarily responsible for Z-contrast variations is Fe. This is confirmed by EDS maps and quantitative EDS point analyses.

3. RESULTS

3.1. Overall and comparative results

Based on previously published analyses and EDS analyses from polished thin sections acquired for this study, most olivines examined in this study cover a range of predominantly forsteritic compositions ($Fo_{83–94}$; Table 1). Only one sample (from the exposed flow surface on the island of Hawai'i) had fayalite content greater than Fa_{17} (Table 1). Olivine in the weathered basalts from the Hawai'ian islands studied here is somewhat more fayalitic ($Fa_{13–32}$) than olivine in the weathered metadunites from the southern Blue Ridge ($Fa_{6–10}$). Where previous analyses are available for comparison, the new EDS analyses of this study conform within a few atom percent to the published analyses.

Freshly exposed surfaces of unweathered olivine exhibit a variety of mechanically produced fracture features. In unweathered samples, interfaces between olivine and the products of pre-weathering aqueous alterations (serpentine, iddingsite) are smooth and featureless (Fig. 1).

Optical petrography of weathered vesicular basalt shows abundant olivine preserved with only slight staining and secondary mineralization of grain boundaries and trans-mineral fractures. Numerous fine-scale parallel "beads-on-a-string" features (which upon higher-magnification examination are revealed to be strings of small etch pits) occur in the immediate vicinity of trans-mineral fractures. Etch pits with similar petrographic characteristics are widespread on olivine in all weathered samples.

In weathered samples, different sample preparations expose olivine etch pits in different ways. Secondary-electron images of natural olivine external surfaces and exposed internal surfaces such as natural fractures reveal conical or funnel-shaped etch pits (Fig. 2; see also Velbel, 1993, Fig. 2). The wide "mouth" of an individual funnel at the imaged surface is often elliptical (Fig. 2). Ellipticity varies in different images but is essentially uniform for multiple etch pits on any individual surface (Fig. 2). Conical etch pits occur as isolated or randomly distributed pits (Fig. 2a–c) and in side-by-side arrays (Fig. 2d). Note that regardless of how they are distributed, all etch pits on a given surface share a common orientation. As adjacent pits enlarge and coalesce, compromise shapes develop at the intersecting pit margins (Fig. 2c). SEI of grain surfaces reveal ubiquitous striations along the walls of the etch pits, pointing toward the apex of each conical pit (Fig. 2). Note also the absence of weathering products in secondary-electron images of etch pits on all samples prepared without physical or chemical treatment to remove products (Figs. 2a, b, and d and 3).

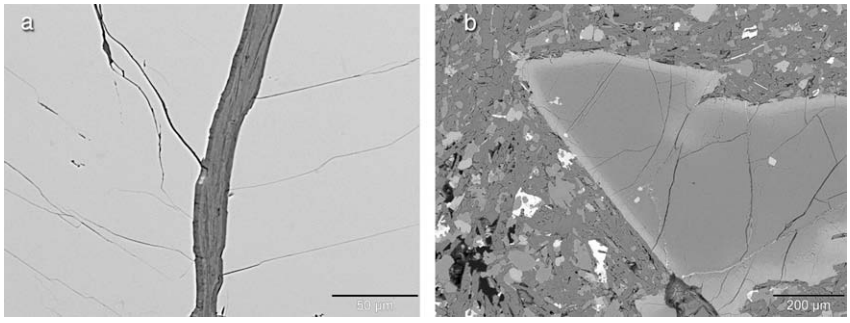

Fig. 1. Olivine–phyllosilicate interfaces in unweathered olivine. BEI of polished thin sections. (a) Olivine (light gray) partially replaced by serpentine (dark gray) in unweathered interior metadunite sample from Webster–Addie complex. Note smooth featureless olivine–serpentine interface and unaltered fractures. Scale bar is 50 µm long. (b) Olivine partially replaced by iddingsite (lighter shade of gray near olivine periphery). Unweathered basalt, Hawai'i. Scale bar is 200 µm long.

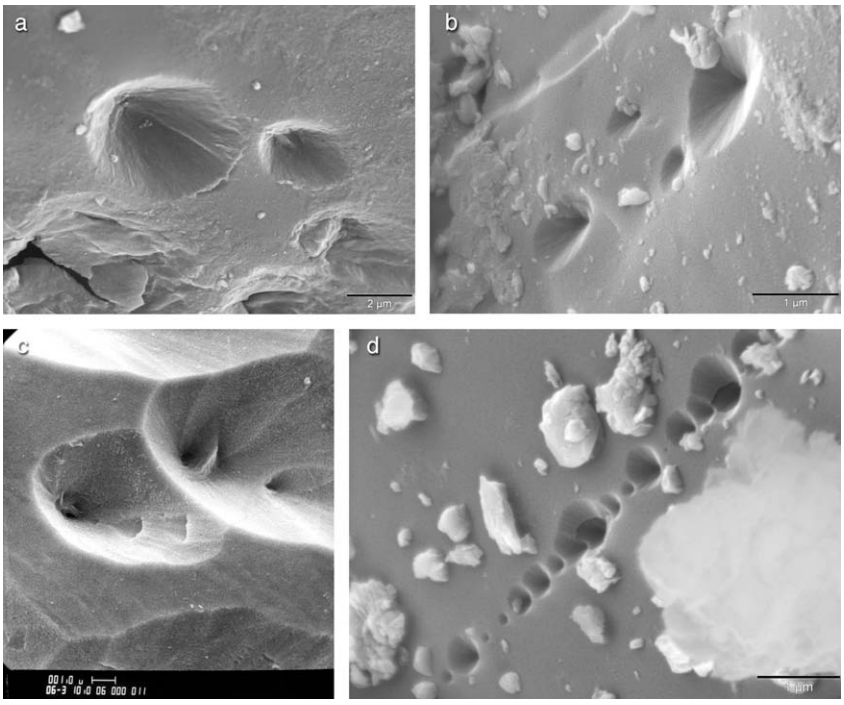

Fig. 2. Conical or funnel-shaped etch pits on weathered olivine. SEI of fragment surfaces. Scale bars are 2 μm long in (a), 1 μm long in (b–d). In (a–c), etch pits on the olivine crystals are all randomly distributed; in (d), etch pits occur in a side-by-side array. All etch pits on a given olivine grain are similarly oriented. The spouts of the funnels point, respectively (a) slightly to the top and left of the line-of-sight; (b) slightly to the right of the line-of-sight; (c) slightly to the left of the line-of-sight; (d) slightly to the right of the line-of-sight. In all these cases, the orientation of the etch pit with respect to the imaged surface results in a low-ellipticity pit margin. Note striations pointing toward the spout in (a–c). Note also the absence of weathering products in etch pits sample imaged in (a), (b) and (d), which were prepared without physical or chemical treatment to remove products (c was ultrasonically cleaned; Velbel and Ranck, 2008). Etch pits range in size from submicron (b and d) to more than 10 μm in long dimension (the largest etch pits in (c), the edges of which are visible at the top and bottom of the field of view c). The samples imaged are from the following localities: (a) Webster–Addie metadunite; (b) slightly weathered corestone interior of Schofield Barracks (Oahu) basalt; (c) Day Book metadunite, North Carolina; (d) slightly weathered corestone interior of Schofield Barracks (Oahu) basalt.

Some fracture surfaces expose diamond-shaped cross-sections of etch pits consisting of pairs of cones sharing a common base (Fig. 3). Such diamond-shaped cross-sections are more commonly exposed in polished thin sections (Figs. 4–10) than on randomly exposed fractures surfaces (Fig. 3). Individual diamond-shaped cross-sections occur at exposed lava-flow surfaces (Fig. 4a), immediately beneath (within a few tens of microns of) metadunite corestone surfaces (Fig. 4b), immediately adjacent to (within a few tens of microns of) fractures in basaltic olivine phenocrysts (Fig. 5), and in the interiors of basaltic olivine phenocrysts transected by fractures (Fig. 8). Arrays of multiple such etch pits joined at the apices of their shorter dimensions appear to be much more common than individual pits in basaltic olivine phenocrysts (Fig. 5) and in metadunite olivine (Figs. 6 and 7) and are similarly distributed relative to fractures and exposed surfaces. Coalescence of *en echelon* diamond-shaped etch-pit cross-sections forms serrated grooves (Figs. 5–8). Some etch pits along edges subparallel (Figs. 6 and 7b) or nearly perpendicular (Fig. 7a) to *en echelon* arrays have triangular, wedge-shaped (half-of-diamond) cross-sections. Wedge-shaped cross-sections are associated with unserpentinized fractures in metadunite olivine (Fig. 7b),

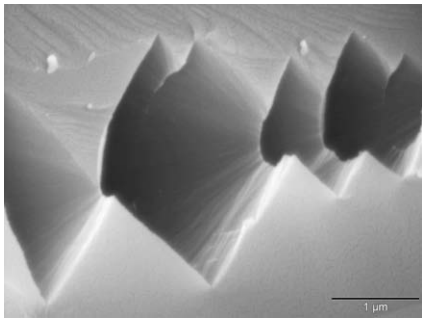

Fig. 3. End-to-end array of pairs of conical etch pits joined base-to-base, all aligned along the apices of the cones. Exposure on a fracture surface parallel to the array shows each base-to-base cone-pair as a diamond-shaped cross-section of the etch-pit pair. Note striations on conical surfaces pointing toward the apex of each cone. Note also the absence of weathering products in etch pits on this sample, prepared without physical or chemical treatment to remove products. SEI of fractured surface, slightly weathered corestone interior, Schofield Barracks (Oahu) basalt. Scale bar is 1 μm long.

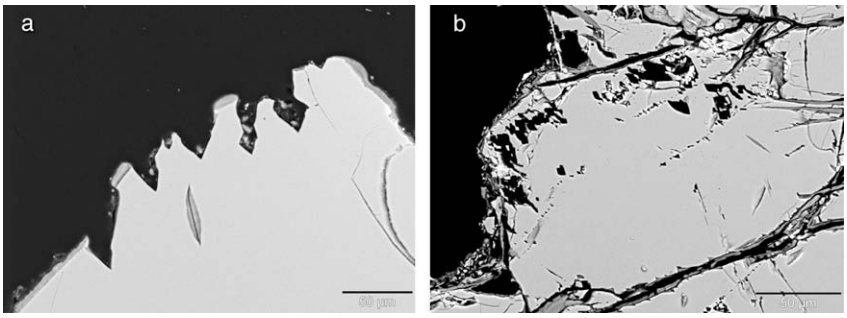

Fig. 4. Olivine exposed and weathered at and near outcrop surfaces. In both images, the limit of finite Z-contrast is the outcrop surface; the black areas at the top and/or left of the fields of view are mounting medium filling space outside the sample. (a) Olivine exposed and weathered at the surface of a young basaltic lava flow on island of Hawai'i. The thin section was cut perpendicular to the lava-flow surface to expose a cross-section through both the outcrop surface and the outermost several centimeters of sample beneath the outcrop surface. The limit of finite Z-contrast is the outcrop surface. Note etch pits on exposed surface. BEI of a polished thin-section oriented to expose a vertical cross-section through the exposed surface of the flow. (b) Olivine (light gray) exposed and weathered at the surface of a visibly rusty corestone from the Webster–Addie metadunite. Note etch pits ~10 μm in size within a few tens of microns of the exposed surface and much smaller etch pits in the grain's interior. Medium gray micaceous material between olivine grains is serpentine and talc. BEI of a polished thin-section oriented to expose a cross-section through the corestone's weathered rind. Scale bars are 50 μm long.

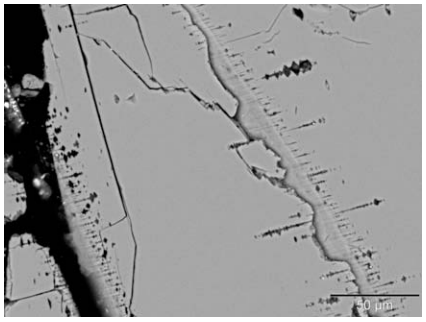

Fig. 5. Olivine shows incipient alteration along wide (black area at left) and narrow (top center to bottom right) trans-mineral fractures. Note diamond-shaped cross-sections of the largest etch pits, most <10 μm in longest dimension, with etch-pit sizes down to the limit of resolution. Many are arranged in *en echelon* arrays, joined at the apices of their shorter dimension. Coalescence forms serrated grooves. Etch pits are empty (no Z-contrast in BEI). BEI of polished thin section from slightly weathered corestone interior, Schofield Barracks (Oahu) basalt. Scale bar is 50 μm long.

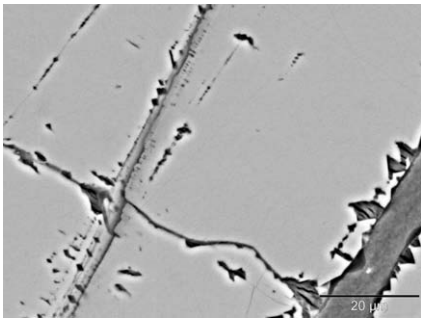

Fig. 6. Arrays of submicron- to micron-scale etch pits associated with fractures and penetrating into olivine (light gray) from fractures. Etch pits several microns in size are associated with meshwork serpentine (medium gray) at lower right. Notice how some etch pits near edges have triangular, wedge-shaped (half-of-diamond) cross-sections. Etch pits along fractures are empty (no Z-contrast; devoid of product); etch pits associated with meshwork serpentine contain lamellar products, similar to serpentine in Z-contrast but different in texture (massive meshwork serpentine; lamellar etch-pit fill). BEI of polished thin section, Webster–Addie metadunite. Scale bar is 20 μm long.

with some occurrences of meshwork serpentine in metadunite (Fig. 9), and with the olivine–iddingsite interface in spheroidally weathered basalt (Fig. 10). Complex etching patterns result from both side-by-side and apex-to-apex coalescence of etch pits (Fig. 11a) and prolonged etching of olivine to a skeletal state (Fig. 11b).

Individual and *en echelon* arrays of diamond-shaped etch-pit cross-sections are observed on fracture surfaces of weathered-rock chips and grain mounts in secondary electron imaging (Fig. 3), but never on the same surfaces with conical pits, suggesting a systematic crystallographic orientation of the pits with surfaces of different orientations exposing different cross-sections through geometrically similar pits (Fig. 12). Individual diamond-shaped cross-sections and *en echelon* arrays of the same basic forms (with adjacent cones joined at their apices) are the dominant form observed in thin sections, optically and in secondary and backscattered electron imagery.

Most etch pits are empty, especially those directly associated with fractures or exposed surfaces. Although some low-Z-contrast products may escape notice in backscattered-electron images, secondary-electron images of grain-surface and etch-pit topography would reveal product morphology if products were present. Such products are generally absent from secondary-electron images of etch-pit topography, even on samples that were not mechanically or chemically treated to remove products. Some etch pits are filled by post-etching secondary/tertiary minerals, often forming product-mineral casts of the etch-pit molds. Because this paper emphasizes primary-mineral corrosion,

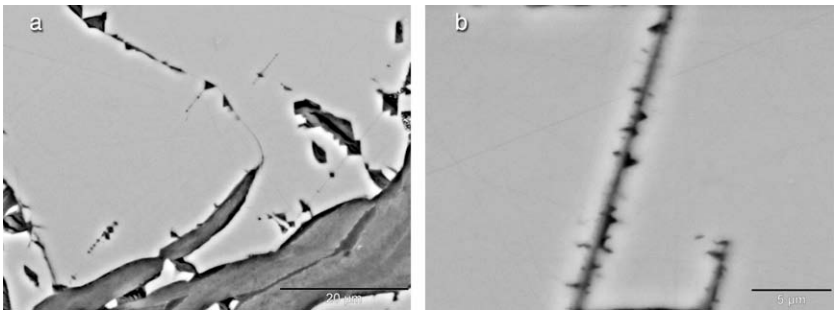

Fig. 7. Arrays of submicron- to micron-scale etch pits associated with fractures and penetrating into olivine (light gray) from fractures. Notice how some etch pits near edges have triangular, wedge-shaped (half-of-diamond) cross-sections. Note several *en echelon* arrays of submicron- to micron-scale etch pits (lower left, upper middle in a). Notice how etch pits along edges subparallel to *en echelon* arrays (b) have triangular, wedge-shaped (half-of-diamond) cross-sections. Interfaces between olivine and meshwork serpentine (medium gray) at lower right in a are sharp, smooth and featureless. Etch pits along and near fractures are empty (no *Z*-contrast; devoid of product). BEI of polished thin section, Webster–Addie metadunite. Scale bar is 20 μm long in (a), 5 μm long in (b).

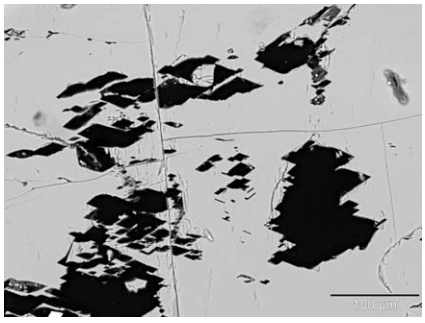

Fig. 8. In the weathered rind around the corestone, diamond-shaped etch pits are larger; the largest individual etch pits approach 100 μm in longest dimension, and even larger dissolution voids are formed by coalescence of adjacent etch pits. Etch pits extend into olivine crystal interiors, and are large enough to penetrate the entire thickness of the thin sections. Individual pits and *en echelon* arrays are common. Most etch pits, especially large pits away from trans-mineral fractures, are devoid of weathering products. BEI of polished thin section from spheroidally weathered shell, Schofield Barracks (Oahu) basalt. Scale bar is 100 μm long.

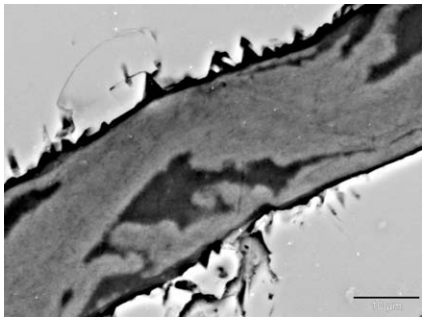

Fig. 9. Wedge-shaped cross-sections through etch pits at grain boundaries between olivine (light gray) and meshwork serpentine (medium-dark gray). BEI of polished thin section, Laurel Creek metadunite. Scale bar is 10 μm long.

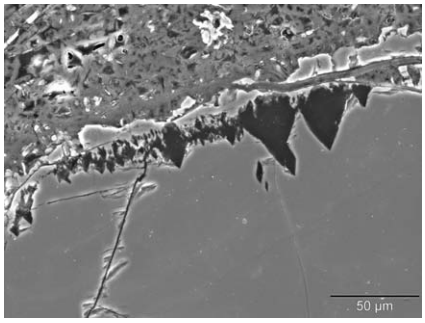

Fig. 10. Wedge-shaped cross-sections of (empty, no *Z*-contrast) etch pits corroding olivine (medium gray, below) from the interface between olivine and iddingsite (slightly lighter shade of gray, immediately above etch pits). Slightly weathered basalt corestone interior, Schofield Barracks (Oahu). SEI of polished thin section. Scale bar is 50 μm long.

details of the secondary minerals will not be discussed further here.

3.2. Specific variations between samples at individual localities

3.2.1. Oahu

Etch pits range in size from less than 1–20 μm (Figs. 2b and d, 3 and 5) in the weathered corestone (WIP = 61; CIA = 66), except immediately beneath iddingsite, where wedge-shaped etch pits are up to 50 μm in size (Fig. 10). At high magnifications in the petrographic microscope, and in SEM, the "beads on a string" are seen to be *en echelon* arrays of diamond-shaped etch pits, aligned and joined along the shorter of the two geometric axes visible in the cross-section view of the thin section. Secondary and backscattered-electron images of polished thin sections reveal more detail including widespread occurrence of arrays of micron- to submicron-scale etch pits that are smaller in size and more widespread near fractures than the larger pits visible by

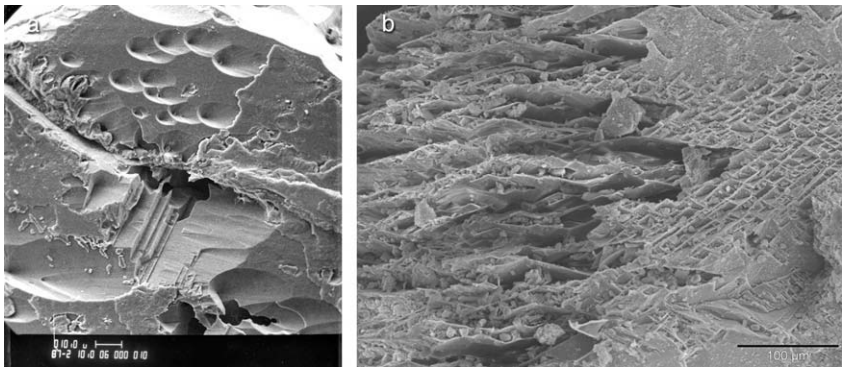

Fig. 11. (a) Complexly sculpted forms resulting from lateral coalescence of side-by-side etch pits and etch pits beneath the apices of the surficial conical pits (left), and other growth, compromise and fracture forms (right). From ultrasonically cleaned weathered rind on Day Book dunite, North Carolina. SEI of fragment surface. Scale bar is 10 μm long. (b) Complexly sculpted forms resulting from coalescence of side-by-side etch pits. Note numerous ~10 μm diamond-shaped pit at right, and ~100 μm-long lenticular pits at left. Olivine from spheroidally weathered shell on basalt, Schofield Barracks (Oahu). SEI of fragment surface. Scale bar is 100 μm long.

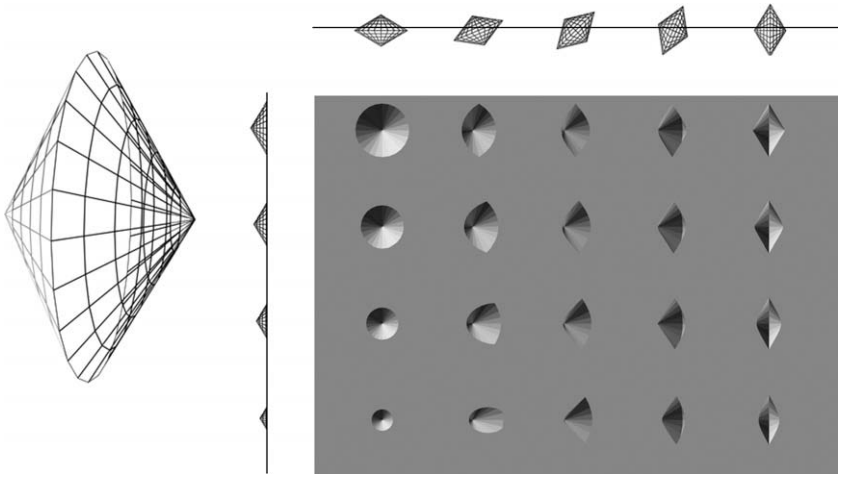

Fig. 12. The basic etch-pit shape is a cone, shown in the wireframe visualization at left. The most common variant is for two such cones to be joined at their bases (bicone, shown at left as two different shades of gray). The matrix at right shows how single and double cones appear when they intersect a planar surface in different orientations (illumination from upper left). Rotation (about a vertical axis) of the cone axis relative to the line-of-sight varies within a row from left to right, in 22.5° increments. Truncation of the pit by a plane at different depths varies from top to bottom. By Aric Velbel.

optical petrography. At more advanced stages of weathering in the spheroidally weathered shell (WIP = 46; CIA = 92), larger pits that penetrate the entire thickness of a thin section are up to ~100 μm in their longest dimension, and even larger dissolution voids are formed by coalescence of adjacent etch pits (Fig. 8).

Most etch pits are devoid of weathering products, even though many etch-pit arrays are within tens of microns of product-filled fractures; however, some pits contain aluminosilicate and/or phosphate alteration products. In both the corestone and the shell, etch pits in partially iddingsitized olivines nucleate at the olivine–iddingsite interface and selectively corrode olivine (Fig. 10). Etch pit forms on olivine surfaces beneath iddingsite are identical to etch pits on product-free olivine surfaces.

3.2.2. Hawai'i

Olivine exposed at the outcrop surface is penetrated to depths of up to 50 μm by individual or coalesced pairs of diamond-shaped etch pits (Fig. 4a). The interior of the same olivine, and olivines in the interior of the sample, are unetched.

3.2.3. Metadunites from southern Appalachian Blue Ridge

Anhedral, conical or funnel-shaped etch pits (Fig. 2a and c), diamond-shaped etch pits in isolation or in *en echelon* arrays (Figs. 4b, 6, and 7a), and wedge-shaped cross-sections through etch pits along fractures (Figs. 6 and 7), grain boundaries, and olivine–serpentine contacts (Figs. 6 and 9) occur on olivine from visibly oxidized weathered rinds on dunite corestones from several metadunite bodies

in the southern Blue Ridge of North Carolina and Georgia. Etch pits are small (submicron to several microns; Figs. 2a, 6, 7, and 9) in metadunite corestones' interiors in all textural associations, and are more numerous and somewhat larger (a few tens of microns; Figs. 2c and 4b) in visibly oxidized weathered rinds. In interiors, some of the larger etch pits associated with serpentine contain product with a different texture than serpentine (lamellar rather than massive; Fig. 6, lower right), but most are empty.

4. DISCUSSION

4.1. Various geometric expressions of olivine etch-pit geometry

Olivine-corrosion etch pits are widespread, and similar in all naturally weathered samples. In naturally weathered samples, different sample preparations expose olivine etch pits in different ways. The basic etch-pit shape on naturally weathered olivine as expressed topographically on surfaces in a variety of orientations imaged by SEI is conical or funnel-shaped (Fig. 2; Velbel, 1993; Velbel and Ranck, 2008). The pointed end (apex of the cone; spout of the funnel) probably defines the (screw or edge; Kirby and Wegner, 1978) dislocation around which the etch pit develops (Young, 1969; Wegner and Christie, 1974; Inoue et al., 1981; Velbel, 1993). The apparent ellipticity of the etch-pit perimeter depends on the angle of intersection of a dislocation and its associated conical pit with the imaged surface (Velbel and Ranck, 2008, Fig. 4; this paper, Figs. 2 and 12); such geometric effects have been elegantly described for etched apatite fission-tracks by Jonckheere and Van den haute (1996). In naturally weathered olivine, the pit–surface intersection angle depends primarily on the orientation of the etched surface. While some surfaces available for microscopic examination on naturally weathered olivine are crystal faces (e.g., grain boundaries of euhedral olivine phenocrysts in volcanic rocks), most surfaces (e.g., fractures, compromise grain boundaries in granular/sucrosic-textured dunites) are not. The greater variety of natural-surface orientations with respect to olivine's crystallographic axes compared to the much smaller number of "standard" orientations used in etching experiments (see below) results in a greater variety of apparent etch-pit shapes on naturally weathered olivine surfaces, even though the shapes of natural pits are all variations on a single conical theme (Fig. 12). As with chemically etched olivines (Kirby and Wegner, 1978), the basic theme of pit morphology does not appear to vary with the orientation of the dislocation relative to the corroded surface. The uniformity of etch pit form on naturally weathered olivines is also consistent with Kirby and Wegner's (1978) observation that both edge and screw dislocations seem to respond similarly to chemical etching in the laboratory.

Some images of grain-surface topography (SEI) reveal diamond-shaped etch pits (e.g., Grandstaff, 1978), some of which, upon closer examination, can be seen to be cross-sections through pairs of cones joined at their bases (funnels joined mouth-to-mouth) (Fig. 3). In BEI and SEI images of polished thin sections, pits of all sizes entirely surrounded by olivine have diamond-shaped cross-sections (Figs. 5 and 8) or shapes formed by the coalescence of multiple diamond-shaped pits (Figs. 4 and 8). Small olivine etch pits at grain boundaries, fractures, and contacts with veins appear as triangular (wedge-shaped) cross-sections that appear to be partial sections through the widely observed diamond-shaped cross-sections (Figs. 6, 7, 9 and 10).

Base-to-base joining of pairs of cones (Fig. 3) is common. Long, serrated grooves formed by apex-to-apex coalescence of small, closely spaced etch pits (Figs. 3, 5 and 6) resemble the parallel etch lamellae (or channels) formed during iddingsitization of olivine and seen in TEM (Eggleton, 1984, 1986; Smith et al., 1987). The etch channels seen in TEM are oriented parallel to the olivine x–y plane, are bridged by saponite syntactic with the parent olivine, and are narrower (a few tens of nanometers across) and more closely spaced (a few tens to hundreds of nanometers apart) than the product-free serrated channels formed by overlap of etch pits observed in this SEM study (Figs. 5 and 7a). TEM images of diamond-shaped etch pits allow two-dimensional cross-sections to be examined in known crystallographic orientations. In a few places, TEM reveals diamond-shaped cross-sections of etch pits (Eggleton, 1986; Banfield et al., 1990; Casey et al., 1993). Viewed by TEM along olivine's y-axis [0 1 0], the diamond-shaped cross-sections are elongate parallel to olivine's z-axis [0 0 1], shorter along olivine's x-axis [1 0 0], and their short axis is aligned with the elongate parallel channels mentioned above (Eggleton, 1986; Banfield et al., 1990). While the largest such pits in published TEM images are smaller (maximum long dimension of ~10 nm) than the smallest that can be individually resolved using conventional SEM (~1 μm; e.g., Figs. 2d, 5 and 6), the similarities of their individual geometry over a range of sizes, and their orientation relationship with the TEM-scale etch channels, are sufficiently similar to suggest that formation of etch-pit arrays like those observed here by SEM is a larger-scale continuation of the same process as inferred at smaller spatial scales from TEM observations. The TEM-scale observations represent an earlier stage of weathering in which pits and grooves are smaller; with continued weathering of olivine the etch-pits grow, become large enough to be discerned by SEM, and coalesce in a spatially larger but geometrically similar manner to their smaller predecessors imaged by TEM.

The few TEM images available of small diamond-shaped pits in olivine are views along [0 1 0], so the dimensions of the pits in the [0 1 0] direction relative to the imaged dimensions in the [1 0 0] and [0 0 1] directions cannot be determined. The qualitative three-dimensional information available from secondary SEM images of naturally etched surfaces (Figs. 2, 3 and 11a) suggests the pits are shortest along the line of the cones' apices [1 0 0], so the bases of the cones (which, in the case of diamond-shaped cross-sections, are joined; Fig. 12) are in the y–z plane, elongate in the [0 1 0] and [0 0 1] directions. The axis of the cones appears to be in the (0 0 1) plane (the plane of the etch channels observed in TEM), possibly along [1 0 0].

4.2. Formation of olivine etch pits exclusively by low-temperature weathering

Aqueous alteration at temperatures higher than Earth-surface ambient weathering temperatures replaces olivine with other minerals (serpentine, iddingsite) but does not produce corrosion features at the retreating olivine surface (Fig. 1). This is consistent with the absence of etch pits associated with olivine–serpentine interfaces in previously published optical petrographic and BSE images of partially serpentinized but unweathered forsteritic olivine (e.g., Nahon et al., 1982b; Schulte et al., 2006). It remains to be established whether the difference between olivine surface textures formed by aqueous alteration at different temperatures is a consequence of the difference in temperature, of the presence of a product, or of different geochemical conditions associated with the product-forming conditions. Details of the relationship between olivine morphology at the interfaces between olivine and phyllosilicate-mineral products of higher-temperature aqueous alteration will be the subject of a future paper.

Olivine-corrosion etch pits are widespread, and similar in all naturally weathered samples. Mammillary surfaces similar to those observed on naturally (Velbel and Ranck, 2008) and experimentally (Grandstaff, 1978) weathered olivine also occur locally. Dissolution features (mammilla and etch pits) on olivine from weathered Day Book, NC dunite and similar samples are consistent with either of two interpretations (1) some olivine corrosion is produced by pre-weathering aqueous alteration (e.g., serpentinization) or (2) small amounts of localized weathering have already affected otherwise-fresh samples (Velbel and Ranck, 2008). However, the present study shows that etch pits form by (low-temperature) weathering, not by higher-temperature aqueous alteration (serpentinization, iddingsitization). The next several paragraphs examine several lines of evidence supporting this inference.

Etch pits are absent from macroscopically unweathered portions of samples (Fig. 1), including the interior of the young Hawai'ian lava flow, and parts of the interiors of several metadunite corestones. Olivine etch pits are clearly associated with chemical and/or mineralogical evidence of weathering, and/or are associated with, or proximal or directly connected to, fractures (the avenues along which aqueous solutions come into contact, and react, with the olivine) or exposed outcrop surface. Origin of etch pits by low-temperature weathering is strongly indicated by occurrences in which corroded olivine occurs only where exposed to the present-day land surface (Fig. 4a) and is absent from unexposed portions of the same olivine or from interior olivines in the same sample.

The size and number of etch pits varies directly with other indicators of weathering. Individual etch-pits range in size from as small as the limit of SEM resolution to as large 80–100 μm in longest dimension, increasing in size with increased weathering. In the Schofield Barracks (Oahu) sample suite, olivines in the corestone are etched (Figs. 2b and d, 3 and 5), because even the corestone is slightly weathered, as indicated by the fact that even the corestone has enriched REE and a negative Ce anomaly (an indicator of weathering under oxidizing conditions; Patino et al., 2003). The increase in etch-pit size in the spheroidally exfoliated shell (Fig. 8) relative to the corestone (Figs. 2b and d, 3 and 5) is directly associated with increased chemical weathering of the shell relative to the corestone as indicated by differences in WIP and CIA between corestone and shell. Although similar chemical weathering indices cannot be applied to ultramafic rocks (because of their low initial alkali, Ca, and alumina abundances), the number and size of etch pits in weathered metadunite olivines increase with proximity to the corestones' exposed surfaces (Fig. 4b), and are associated with visible oxidation absent from unweathered interiors.

Etch pits in the interiors of serpentinized metadunites most likely formed by weathering. Even if small etch pits form by pre-weathering aqueous alterations as suggested by Velbel and Ranck (2008), weathering is clearly responsible for continued enlargement of etch pits, as the pit dimensions in the visibly and/or chemically more weathered samples are noticeably larger than in the corresponding less weathered samples.

A weathering origin of olivine etch pits in serpentinized dunites is more clearly shown by etch pits associated with otherwise unaltered fractures (Figs. 6 and 7). Fractures would have been serpentinized had fracturing preceded serpentinization. Therefore, unserpentinized fractures (and the etch pits on them and directly associated with them) post-date serpentinization. Etch pits on serpentine-free fractures in partially serpentinized rocks post-date serpentinization and are probably features of incipient corrosion, likely associated with the more extensive corrosion at the exposed surfaces of many of the same samples (Fig. 4b). Wedge-shaped etch pits along post-serpentinization fractures but not at olivine–serpentine interfaces (indicating post-serpentinization origin of the pits) with a size, shape, orientation, and distribution similar to those reported here have been imaged but not remarked upon by Nahon et al. (1982b; their Fig. 5A).

Small olivine etch pits occur at some olivine–serpentine interfaces (Fig. 6 lower right; Fig. 9). This suggests that corrosion of olivine is facilitated by fluids entering the rock along the olivine–serpentine grain boundaries. Serpentine occurring as meshwork and veins likely allows fluids access to greater depths within partially serpentinized metadunites than would be the case in the absence of meshwork serpentine. Deeper macroscopic-scale weathering of serpentinized ultramafic rocks relative to immediately adjacent unserpentinized ultramafics is known from nickel laterite deposits (e.g., the Bulong Ni-laterite of Western Australia; Elias et al., 1981).

Occurrences of serpentinization (Fig. 1a) and iddingsitization (Fig. 1b) lacking etch pits indicate that those high-temperature alterations occur without etching olivine. Associations of small etch pits with serpentine (Figs. 6 and 9) and iddingsite (Fig. 10) can all be explained by corrosion of olivine after, rather than during, higher-temperature alteration. Weathering-produced etch forms superimposed on already serpentinized and iddingsitized olivine are morphologically identical to those formed by weathering where products of previous alteration are ab-

sent. In summary, all occurrences of olivine etch pits in the naturally weathered olivines examined here can be explained as being related to ingress of low-temperature Earth-surface aqueous solutions to the site of olivine etching.

4.3. Uniformity of olivine etching during natural weathering

Olivine-corrosion textures are similar in all sample suites, despite differences in crystallization and weathering/exposure ages, and regolith history. Olivine etch pits in all volcanic- and metamorphic-rock samples studied here are morphologically identical to those shown by Velbel (1993) from a sample of weathered Hawai'ian volcanic rock with unequivocal trace-element geochemical signatures of low-temperature weathering under oxidizing conditions (Patino et al., 2003). This suggests that olivine in volcanic and metamorphosed rocks is similarly corroded regardless of differences in primary crystallization, subsequent deformation, and pre-weathering alteration of the olivine in the different parent-rock types. Diamond-shaped cross-sections through biconical etch pits occur on the most (Fig. 4a) and least (Figs. 4b and 6) fayalitic olivines examined for this study, indicating that, at least over the compositional range examine here, differences in etching with composition are negligible.

4.4. Implications for reaction mechanism and rate-determining process

All experimental studies of ambient temperature olivine dissolution kinetics (including those reviewed by Velbel (1999), and more recent experimental papers; Awad et al., 2000; Rosso and Rimstidt, 2000; Pokrovsky and Schott, 2000a,b; Oelkers, 2001; Liu et al., 2006; Olsen and Rimstidt, 2007) suggest that olivine dissolution is interface-limited, with the rate-determining step being the breakdown of a surface activated complex. Morphological evidence of widespread olivine etching under natural ambient conditions is consistent with the overall interface-limited rate-limiting process determined experimentally, as is the case for most other common rock-forming silicate minerals (Wilson, 1975, 2004; Berner and Holdren, 1977, 1979; Berner, 1978; Berner et al., 1980; Berner and Schott, 1982; Velbel, 1986, 1993, 1999, 2007) and less common silicates under specific circumstances (Velbel, 1984; Velbel et al., 1996, 2007).

Etch pits on naturally weathered feldspars (Berner and Holdren, 1977, 1979; Velbel, 1983, 1986; Lee and Parsons, 1995; Lee et al., 1998, 2007; Parsons et al., 2005; Brown and Lee, 2007) and garnets (Velbel, 1984; Velbel et al., 2007), and chemically etched olivines (e.g., Grossman et al., 1971; Wegner and Christie, 1974, 1976; Kirby and Wegner, 1978) are commonly euhedral. However, the conical surfaces of olivine etch pits do not conform to individual crystal planes and faces of the dissolving mineral's structure. In this, olivine etch pits more closely resemble those on chain-silicates (pyroxenes, amphiboles; Berner et al., 1980; Berner and Schott, 1982; Velbel, 2007), on which the anisotropic morphology of etch-pits and between-pit remnants is related in orientation to the parent mineral's crystallographic axes, but the etching-exposed surfaces are not themselves crystal planes.

4.5. Comparison with putative biogenic features in naturally exposed olivine

The conical (Fig. 2) and biconical (Figs. 3, 4a and 8) etch pits, and *en echelon* arrays of etch pits (Figs. 3, 5, 6 and 7a) formed by natural weathering of forsteritic olivine do not resemble the long (to 100 μm), narrow (1–3 μm) curved tunnels or the larger, irregular-walled galleries found associated with nucleic acids and other indicators of microbial habitation in glass and olivine by Fisk et al. (2006). Etch pits formed by natural weathering of olivine differ from biotic corrosion features described by Fisk et al. (2006) in being non-uniform in size in individual samples, such that elongate cavities produced by dissolution forming *en echelon* etch pits vary in diameter along the length of the cavities. The morphological similarity between the etch pits observed on naturally weathered forsterite (Velbel, 1993; Velbel and Ranck, 2008; this study) and etch pits formed by strong (inorganic) etchants in support of dislocation studies (Wegner and Christie, 1974, 1976; Kirby and Wegner, 1978; Inoue et al., 1981; Section 4.6.4 below) suggests that either natural weathering of olivine is largely abiotic, or that the naturally weathered samples examined here were affected by biotic weathering that produced etch-pit forms similar to abiotically etched olivine and different from the biotic textures reported by Fisk et al. (2006). The latter seems unlikely.

4.6. Comparison with experimental etching

There is a considerable literature on laboratory dissolution-kinetics experiments of olivine-group minerals, but very little of this literature addresses any relationship between weathering rate-processes and SEM-scale grain-surface textural features. This section compares the etch pits observed here on naturally weathered forsteritic olivine with surface textures produced by three types of experiments (1) abiotic/inorganic experiments under broadly natural conditions (dissolution-kinetics experiments); (2) biotically mediated experiments; (3) etching under extreme conditions not intended to simulate nature (etching studies of defects/dislocations). Similarities and differences in weathering/corrosion textures between forsteritic and fayalitic olivines are also discussed.

4.6.1. Comparison with textures formed in abiotic/inorganic laboratory dissolution-kinetics experiments

Grandstaff (1978) observed mammillary surfaces and *en echelon* lenticular etch pits on forsterite grains experimentally dissolved at room temperature and pH 2.6. Mammillary surfaces were also observed on pre-experiment olivine grains (and may therefore not have been formed during experimental alteration), but etch pits produced experimentally by Grandstaff (1978) were very similar in size, form and distribution to those imaged by Velbel (1993), Velbel and Ranck (2008) and this paper from naturally weathered olivine.

A number of papers on experimental dissolution of olivine under weathering conditions contain SEM images of etch pits similar to those observed in nature (e.g., Velbel, 1993; Velbel and Ranck, 2008; and this paper). Etch pits resembling those on naturally weathered olivine are formed only by experiments in acidic solutions (e.g., pH < 3; Grandstaff, 1978; Seyama et al., 1996; Awad et al., 2000; Pokrvosky and Schott, 2000a,b; Santelli et al., 2001; Welch and Banfield, 2002), and only under abiotic conditions (Santelli et al., 2001; Welch and Banfield, 2002). In many of these cases, other experiments were performed by the same researchers at other conditions (e.g., higher pH), and etch pits like those formed in nature were not formed under those conditions. Similar observations are reported by multiple research groups; olivine etch pits resembling those formed in nature form during laboratory experiments only at strongly acidic conditions. This may be simply because dissolution at higher (e.g., circum-neutral and higher) pH is simply too slow (e.g., see summary of experimentally determined olivine dissolution rates in Olsen and Rimstidt, 2007) to produce etch pits of any geometry on experimental timescales.

4.6.2. Similarities and variations of corrosion features with olivine composition

The morphology of experimentally produced etch pits appears not to vary much with the composition of the olivine, within the range of olivine compositions examined here ($Fo_{68–94}$). Secondary electron (topographic) images of experimentally dissolved forsteritic olivine show randomly distributed but identically oriented elongate etch pits of varying shapes (Pokrovsky and Schott, 2000a,b, their Fig. 3b) including elliptical (Seyama et al., 1996, their Fig. 6b) and almond-shaped (Awad et al., 2000, their Fig. 1d), and *en echelon* arrays of diamond-shaped cross-sections (Grandstaff, 1978, his Fig. 2e), many of which are morphologically similar to natural (forsteritic) olivine etch pits illustrated by Velbel (1993), Velbel and Ranck (2008), and this paper. Lower-magnification images of etch pits on fayalitic olivine show (1) randomly distributed but identically oriented elongate etch pits, some almond-shaped with pointed ends (Seyama et al., 1996, their Fig. 5), some elliptical with rounded ends (Welch and Banfield, 2002, their Fig. 1b) and (2) elliptical etch pits with rounded ends laterally aligned in chains (Santelli et al., 2001, their Fig. 4b), similar in variety, distribution and orientation to those on natural olivine illustrated by Velbel (1993), Velbel and Ranck (2008), and this paper.

Some features of experimentally weathered fayalitic olivine differ from the etch pits discussed in the previous paragraph. Experimentally dissolved fayalitic olivine exhibits a greater tendency toward grooved or striated appearance (Seyama et al., 1996; Santelli et al., 2001; Welch and Banfield, 2002) than either experimentally dissolved forsteritic olivine (Grandstaff, 1978; Awad et al., 2000; Pokrovsky and Schott, 2000a,b) or naturally weathered olivine of the predominantly forsteritic compositions examined to date (Velbel, 1993; Velbel and Ranck, 2008; this paper). The occurrence of grooved/striated surfaces on experimentally altered fayalite and the absence of such surfaces from forsterite may be a consequence of different defect/dislocation phenomena in fayalitic and forsteritic olivines. Intergrown lamellae of laihunite (a structure similar to olivine but with oxidized Fe and vacancies, formed during subsolidus oxidation of olivine; Banfield et al., 1990) in volcanic olivine of intermediate composition ($Fo_{35–85}$) impart compositional alteration resistance to laihunitized volumes of olivine (most affected at grain margins; Banfield et al., 1990). This type of compositional imperfection in natural olivine influences weathering in a different manner than defects, edge or screw dislocations, and volumes involving coherency-strain at two-phase interfaces (Banfield et al., 1990). Similar defects occur in more forsteritic ($Fo_{85–91}$) mantle olivine (Banfield et al., 1992). Such lamellar defects are most abundant at grain margins, suggesting origin by an episode of oxidation after olivine crystallization (subsolidus; Banfield et al., 1990).

One consequence of alteration-resistant laihunite lamellae is that low-temperature deuteric alteration and weathering remove the olivine between the laihunite lamellae producing an elongate, channel- or groove-like morphology identical in scale and orientation with the etch channels or lamellae previously reported in TEM studies of naturally weathered olivine (Eggleton, 1984, 1986; Smith et al., 1987; Banfield et al., 1990). Such TEM-scale etch channels (commonly ~10 nm across) occur in naturally weathered olivines of a variety of compositions ($Fo_{81–86}$, Eggleton, 1984; Fo_{80}, Smith et al., 1987; $Fo_{35–85}$, Banfield et al., 1990), and in experimentally weathered fayalite where they are directly associated with wider and more widely spaced but otherwise morphologically related SEM-scale grain-surface features (Welch and Banfield, 2002; see also SEM imagery from same samples in Santelli et al. (2001)). However, despite the wide range of olivine compositions to exhibit etch channels at TEM scales, SEM-scale features that might be equivalent results of differential weathering of compositionally different lamellae without associated lattice strain appear to be very uncommon in the naturally weathered, typically forsteritic olivines examined in this study. Fig. 5 shows numerous parallel grooves, the largest of which are contiguous with *en echelon* arrays of biconical etch pits; the grooves themselves resemble the grooves observed in TEM on naturally (Eggleton, 1984, 1986; Smith et al., 1987; Banfield et al., 1990) and experimentally (Welch and Banfield, 2002) dissolved olivines, except that the grooves visible in SEM (Fig. 5) are much larger and farther apart than those observed in TEM. These are the only SEM-scale surface textures that may be related to the grooves formed by preferential weathering of olivine relative to extended strain-free imperfections in the form of alteration-resistant laihunite lamellae. Most etch pits in the naturally weathered olivines examined here more closely resemble pits formed experimentally at edge and screw dislocations, with their associated lattice strain (Kirby and Wegner, 1978; Brantley et al., 1986).

Using SEM, Seyama et al. (1996) observed elongate etch pits and grooves formed by end-to-end coalescence of smaller etch pits on both fayalite and forsterite acid-leached at room temperature (none of the imaged features were present in images acquired from grains prior to leaching). Awad

et al. (2000) formed a variety of etch pits on artificially produced surfaces of gem-quality forsteritic olivine in highly acidic solutions (pH 1–2) at a range of temperatures from 23 to 90 °C, with geometries like those reported from naturally weathered olivine by Velbel (1993), Velbel and Ranck (2008) and this paper (including diamond-shaped etch pits on (0 0 1) and elongate in the [0 1 0] direction). By careful preparation and measurement of their experimentally prepared solids before, during and after their experiments, Awad et al. (2000) were able to measure olivine dissolution rates in three different crystallographic directions, and to determine the temperature dependence (Arrhenius activation energy) of the reaction rate in each of the three directions. From their data, it might eventually be possible to use etch-pit geometry on olivines to determine the temperature at which the olivine corroded.

4.6.3. Comparison with textures formed in biotically mediated laboratory experiments

Longazo et al. (2001, 2002a,b) found submicron-scale "regular" (e.g., triangular; Longazo et al., 2001, their Fig. 2) etch pits on experimentally altered forsterite. Longazo et al. (2002b) reported "regular" pits to be products of experimental inorganic alteration of forsterite, and irregularly shaped cavities with associated biofilms or bacterial forms as products of bacterially mediated experimental alteration. Bacteria tend to preferentially colonize pre-existing abiotic etch pits on forsteritic olivine, but only small (submicron) etch features occur on biotically etched forsterite (Longazo et al., 2001, 2002a,b), and these are visible only with field-emission SEM (FE-SEM), that permits resolutions and magnifications an order of magnitude higher than possible using the conventional SEMs used in this study. Direct comparison with the biotically mediated results of Longazo et al. (2001, 2002a,b) will require future FE-SEM observations of naturally weathered forsterites like those examined here.

The Fe-reducing bacteria used in published fayalite dissolution experiments appear to produce grooved/striated surfaces (Santelli et al., 2001; Welch and Banfield, 2002) that are morphologically indistinguishable from those formed by abiotic experimental alteration of fayalite (Seyama et al., 1996). The absence of fayalitic olivines from this study precludes further comparison at this time.

4.6.4. Comparison with textures formed by extreme etchants

A number of papers reported experimental etching of olivine using strong acids, bases, and complexing agents, in support of studies of defects, dislocations, rock and mineral deformation, and cosmic-ray exposure tracks in minerals (Young, 1969; Grossman et al., 1971; Wegner and Christie, 1974, 1976; Kirby and Wegner, 1978; Inoue et al., 1981). In these experiments, euhedral or cleaved single crystals or artificially polished surfaces of known low-index crystallographic orientation – usually (1 0 0) or (0 1 0), less commonly (0 0 1) – were etched to discern the different pit shapes (etch figures) that result on different crystals in different crystallographic directions. Randomly oriented conical etch tracks were interpreted as etched cosmic-ray tracks in the same etched lunar olivines that exhibit crystallographically bounded and oriented rectangular dislocation etch pits of shapes characteristic of olivine (1 0 0) and (0 1 0) surfaces (Grossman et al., 1971). Experimentally produced rectangular pyramidal pits on (0 1 0) and (1 0 0) are elongate in the [0 0 1] and [0 1 0] directions, respectively (Wegner and Christie, 1974, 1976; Kirby and Wegner, 1978); a few occurrences of square-based pyramidal pits have also been reported. Some studies found that different etchants are required on different crystal planes; the (0 0 1) surface of olivine was particularly difficult to etch (Young, 1969; Wegner and Christie, 1974, 1976). Oval- and diamond-shaped etch pits elongate in the [0 1 0] direction and shorter in the [1 0 0] direction, and arrays of diamond-shaped pits aligned either in the [1 0 0] direction or in some other orientation in the x–y plane, have been produced experimentally on (0 0 1) surfaces (Wegner and Christie, 1974, 1976; Kirby and Wegner, 1978; Inoue et al., 1981). All these observations from etching experiments are consistent with the elongation of diamond-shaped etch pits and their alignment with etch channels imaged in TEM (Eggleton, 1986; Banfield et al., 1990) and with the pit orientations inferred from the morphological observations of this study.

5. CONCLUSIONS

Olivine phenocrysts in Hawai'ian volcanic rocks from several volcanic centers and regolith/outcrop settings, and tectonized olivines from several metadunite bodies in the southern Appalachian Blue Ridge, are all similarly corroded by conical (funnel-shaped) etch pits occurring as individual pits, base-to-base pairs of cone-shaped pits, or *en echelon* arrays. Etch pits occur in samples with chemical and/or mineralogical evidence of weathering, and/or are associated with, or proximal or directly connected to, fractures or exposed outcrop surface. Etch pits form by weathering, and are not inherited from pre-weathering aqueous alteration (e.g., serpentinization, iddingsitization) of these parent rocks.

Secondary-electron images of grain-surface topography reveal individual funnel-shaped etch pits (each with a pointed end, that probably defines the dislocation around which the etch pit develops), base-to-base pairs of cone-shaped pits yielding diamond-shapes when exposed in cross-section, and chains of diamond-shaped pits aligned and joined laterally along the shorter of the two geometric axes exposed by the intersection of the pits with the surface of the olivine. The smallest etch-pit arrays visible in conventional SEM exhibit etch-pit shapes, orientations, and alignment very similar to those of even smaller features previously reported from TEM investigations of olivine weathering.

Etch-pit walls are not crystal faces or planes, but the orientations of the pits are crystallographically controlled. Conical etch pits in any individual image may be randomly or regularly distributed, but all have the same orientation. Biconical etch pits are shortest along the line of the cones' apices [1 0 0], so the bases of the cones (which, in the case of diamond-shaped cross-sections, are joined) are in the y–z plane, elongate in the [0 1 0] and [0 0 1] directions. Dia-

mond-shaped cross-sections through biconical etch pits are elongate parallel to olivine's *z*-axis [0 0 1] and shorter along olivine's *x*-axis [1 0 0]; *en echelon* arrays of etch pits are aligned along [1 0 0].

Natural weathering of olivine is surface-reaction-limited. Many etch pits are devoid of weathering products. Similarity of corrosion forms from naturally weathered olivine from multiple igneous and metamorphic parent-rock bodies suggests that olivine weathers in the same manner regardless of its specific crystallization/recrystallization history, eruption/weathering/exposure ages of the olivine's host rock, and the local regolith history.

ACKNOWLEDGMENTS

I thank Susan J. Wentworth, Theresa Longazo, Lina C. Patino, and Nilton O. Renno for helpful discussions at various stages of this project; current and former MSU graduate students Jason R. Price, Jennifer A. Wade, Angela R. Donatelle, Daniel R. Snyder, and Anna I. Losiak, for helpful discussions and assistance in the laboratory; and Alan Pooley (Yale Peabody Museum), Ewa Danielewicz (Michigan State University Center for Advanced Microscopy), and Anna Losiak for assistance with some of the scanning electron microscopy. Early versions of this work were presented at several Lunar and Planetary Science Conferences, the Eighth Symposium on the Geochemistry of the Earth's Surface (GES-8), and the Lunar and Planetary Institute Workshop on Modeling Martian Hydrous Environments; I thank D.S. McKay, L.M. Spencer, A. White, S. Gislason, J. Ganor, A. Treiman, H. Newsom, and J.C. Dixon for helpful discussions at those meetings. I am grateful to Maria Mange, David Wright, Lina Patino, and Dan Snyder for their many helpful comments on earlier versions of this paper. Thoughtful comments by Associate Editor Jacques Schott and three anonymous reviewers were very helpful and are greatly appreciated. Aric M. Velbel assisted with Fig. 12, and Harley Seeley prepared the final image files; I thank both for helping bring this presentation to completion. Collection, preparation & preliminary petrographic characterization of some weathered basalt samples from the island of Hawai'i were supported by NSF Grant EAR 91-17099 & EAR 94-17325 (R.A. Berner, P.I.). Geochemical characterization of incipiently weathered volcanic rocks was supported by NSF Grant EAR 99-09493 (L.C. Patino, P.I.; M.A. Velbel, co-P.I.). All other aspects of this research were supported by NASA Grant NAG 9-1211 (M.A. Velbel, P.I.) and NASA Mars Fundamental Research Program Grant NNG05GL77G (M.A. Velbel, P.I.).

REFERENCES

Awad A., Koster van Groos A. F. and Guggenheim S. (2000) Forsteritic olivine: effect of crystallographic direction on dissolution kinetics. *Geochim. Cosmochim. Acta* **64**, 1765–1772.

Banfield J. F., Veblen D. R. and Jones B. F. (1990) Transmission electron microscopy of subsolidus oxidation and weathering of olivine. *Contrib. Mineral. Petrol.* **106**, 110–123.

Banfield J. F., Dyar M. D. and McGuire A. V. (1992) The defect structure of oxidized mantle olivine from Dish Hill, California. *Am. Mineral.* **77**, 977–986.

Berner R. A. (1978) Rate control of mineral dissolution under earth surface conditions. *Am. J. Sci.* **278**, 1235–1252.

Berner R. A. and Cochran M. F. (1998) Plant-induced weathering of Hawaiian basalts. *J. Sed. Res.* **68**, 723–726.

Berner R. A. and Holdren G. R. (1977) Mechanism of feldspar weathering: some observational evidence. *Geology* **5**, 369–372.

Berner R. A. and Holdren G. R. (1979) Mechanism of feldspar weathering. II. Observations of feldspars from soils. *Geochim. Cosmochim. Acta* **43**, 1173–1186.

Berner R. A. and Schott J. (1982) Mechanism of pyroxene and amphibole weathering. II. Observations of soil grains. *Am. J. Sci.* **282**, 1214–1231.

Berner R. A., Sjöberg E. L., Velbel M. A. and Krom M. D. (1980) Dissolution of pyroxenes and amphiboles during weathering. *Science* **207**, 1205–1206.

Brantley S. L., Crane S. R., Crerar D. A., Hellman R. and Stallard R. (1986) Dissolution at dislocation etch pits in quartz. *Geochim. Cosmochim. Acta* **50**, 2349–2361.

Brown D. J. and Lee M. (2007) From microscopic minerals to global climate change? *Geol. Today* **23**, 172–177.

Carpenter J. R. and Phyfer D. W. (1975) Olivine compositions from southern Appalachian ultramafics. *Southeastern Geol.* **16**, 169–172.

Casey W. H., Banfield J. F., Westrich H. R. and McLaughlin L. (1993) What do dissolution experiments tell us about natural weathering? *Chem. Geol.* **105**, 1–15.

Cochran M. F. and Berner R. A. (1996) Promotion of chemical weathering by higher plants; field observations on Hawaiian basalts. *Chem. Geol.* **132**, 71–77.

Delvigne J. (1998) *Atlas of Micromorphology of Mineral Alteration and Weathering*. The Canadian Mineralogist, Special Publication 3, 495 pp.

Delvigne J., Bisdom E. B. A., Sleeman J. and Stoops G. (1979) Olivines, their pseudomorphs and secondary products. *Pédologie* **29**, 247–309.

Eggleton R. A. (1984) Formation of iddingsite rims on olivine: a transmission electron microscope study. *Clay Clay Mineral.* **32**, 1–11.

Eggleton R. A. (1986) The relation between crystal structure and silicate weathering rates. In *Rates of Chemical Weathering of Rocks and Minerals* (eds. S. M. Colman and D. P. Dethier). Academic Press, Orlando, Florida, pp. 21–40.

Elias M., Donaldson M. J. and Giorgetta N. E. (1981) Geology, mineralogy, and chemistry of lateritic nickel–cobalt deposits near Kalgoorlie, Western Australia. *Econ. Geol.* **76**, 1775–1783.

Feiss P. G., Maybin, III, A. H., Riggs S. R. and Grosz A. E. (1991) Mineral resources of the Carolinas. In *The Geology of the Carolinas* (eds. J. W. Horton Jr. and V. A. Zullo). The University of Tennessee Press, pp. 319–345.

Fisk M. R., Popa R., Mason O. U., Storrie-Lombardi M. C. and Vicenzi E. P. (2006) Iron–magnesium silicate bioweathering on Earth (and Mars?). *Astrobiology* **6**, 48–68.

Goldich S. S. (1938) A study in rock weathering. *J. Geol.* **46**, 17–58.

Grandstaff D. E. (1978) Changes in surface area and morphology and the mechanism of forsterite dissolution. *Geochim. Cosmochim. Acta* **42**, 1899–1901.

Grossman J. J., Ryan J. A., Mukherjee N. R. and Wegner M. W. (1971) Microchemical, microphysical, and adhesive properties of lunar material. In *Proc. Second Lunar Sci. Conf.*, vol. 3, pp. 2153–2164.

Hatcher, Jr., R. D., Hooper R. J., Petty S. M. and Willis J. D. (1984) Structure and chemical petrology of three southern Appalachian mafic–ultramafic complexes and their bearing upon the tectonics of emplacement and origin of Appalachian ultramafic bodies. *Am. J. Sci.* **284**, 484–506.

Hatcher, Jr., R. D., Merschat A. J. and Thigpen J. R. (2005) Blue Ridge primer. In *Blue Ridge Geology Geotraverse East of the Great Smoky Mountains National Park Western North Carolina* (eds. R. D. Hatcher Jr. and A. J. Merschat). Carolina Geological Society Annual Field Trip Guidebook, pp. 1–24.

Hay R. L. (1959) Origin and weathering of late Pleistocene ash deposits of St. Vincent, B.W.I.. *J. Geol.* **67**, 65–87.

Inoue T., Komatsu H., Hosoya S. and Takei H. (1981) Defect structures of synthetic olivine. *J. Cryst. Growth* **55**, 307–316.

Jonckheere R. and Van den haute P. (1996) Observations on the geometry of etched fission tracks in apatite: implications for models of track revelation. *Am. Mineral.* **81**, 1476–1493.

Kirby S. H. and Wegner M. W. (1978) Dislocation substructure of mantle-derived olivine as revealed by selective chemical etching and transmission electron microscopy. *Phys. Chem. Mineral.* **3**, 309–330.

Lasaga A. C. (1998) *Kinetic Theory in the Earth Sciences*. Princeton University Press, Princeton, NJ, 811p.

Lee M. R. and Parsons I. (1995) Microtextural controls of weathering of perthitic alkali feldspars. *Geochim. Cosmochim. Acta* **59**, 4465–4488.

Lee M. R., Hodson M. E. and Parsons I. (1998) The role of intragranular microtextures and microstructures in chemical and mechanical weathering: direct comparisons of experimentally and naturally weathered alkali feldspars. *Geochim. Cosmochim. Acta* **62**, 2771–2778.

Lee M. R., Brown D. J., Smith C. L., Hodson M. E., MacKenzie M. and Hellmann R. (2007) Characterization of mineral surfaces using FIB and TEM: a case study of naturally weathered alkali feldspars. *Am. Mineral.* **92**, 1383–1394.

Liu Y., Olsen A. A. and Rimstidt J. D. (2006) Mechanism for the dissolution of olivine series minerals in acidic solutions. *Am. Mineral.* **91**, 455–458.

Longazo T. G., Wentworth S. J., Southam G., McKay D. S. and Clemett S. J. (2001) Olivine weathering: abiotic versus biotic processes as possible biosignatures. *Lunar Planet. Sci. XXXII*. #2013 (abstr.).

Longazo T. G., Wentworth S. J., Southam G. and McKay D. S. (2002) Microbial weathering of olivine. *Lunar Planet. Sci. XXXII*. #1985 (abstr.).

Longazo T. G., Wentworth S. J., Southam G. and McKay D. S. (2002b) Observations of experimental microbial etch textures of olivine: a potential biosignature? *Geol. Soc. Am. Abstr. Programs* **34**, 493.

McSween Jr. H. Y. and Hatcher Jr. R. D. (1985) Field Trip #4: Ophiolites(?) of the Southern Appalachian Blue Ridge. In *Field Trips in the Southern Appalachians. Studies in Geology*, vol. 9 (ed. N. B. Woodward). University of Tennessee, Department of Geological Sciences, pp. 144–170.

Miller, III, R. (1953) The Webster–Addie ultramafic ring, Jackson County, North Carolina, and secondary alteration of its chromite. *Am. Mineral.* **38**, 1134–1147.

Morton A. C. and Hallsworth C. R. (1999) Processes controlling the composition of heavy minerals in sandstones. *Sed. Geol.* **124**, 3–29.

Nahon D., Colin F. and Tardy Y. (1982a) Formation and distribution of Mg, Fe, Mn-smectites in the first stages of the lateritic weathering of forsterite and tephroite. *Clay Mineral.* **17**, 339–348.

Nahon D., Paquet H. and Delvigne J. (1982b) Ultramafic rocks weathering and nickel concentration in Western Ivory Coast. *Econ. Geol.* **77**, 1159–1175.

Nesbitt H. W. and Wilson R. E. (1992) Recent chemical weathering of basalts. *Am. J. Sci.* **292**, 740–777.

Oelkers E. H. (2001) An experimental study of forsterite dissolution rates as a function of temperature and aqueous Mg and Si concentrations. *Chem. Geol.* **175**, 485–494.

Ollier C. D. (1967) Spheroidal weathering, exfoliation and constant volume alteration. *Z. Geomorphol.* **11**, 103–108.

Ollier C. D. (1971) Causes of spheroidal weathering. *Earth Sci. Rev.* **7**, 127–141.

Olsen A. A. and Rimstidt J. D. (2007) Using a mineral lifetime diagram to evaluate the persistence of olivine on Mars. *Am. Mineral.* **92**, 598–602.

Parker A. (1970) An index of weathering for silicate rocks. *Geol. Mag.* **107**, 501–504.

Parsons I., Thompson P., Lee M. R. and Cayzer N. (2005) Alkali feldspar microtextures as provenance indicators in siliciclastic rocks and their role in feldspar dissolution during transport and diagenesis. *J. Sed. Res.* **75**, 921–942.

Patino L. C., Velbel M. A., Price J. R. and Wade J. A. (2003) Trace element mobility during spheroidal weathering of basalts and andesites in Hawaii and Guatemala. *Chem. Geol.* **202**, 343–364.

Pokrovsky O. P. and Schott J. (2000a) Forsterite surface composition in aqueous solutions: a combined potentiometric, electrokinetic, and spectroscopic approach. *Geochim. Cosmochim. Acta* **64**, 3299–3312.

Pokrovsky O. P. and Schott J. (2000b) Kinetics and mechanism of forsterite dissolution at 25 °C and pH from 1 to 12. *Geochim. Cosmochim. Acta* **64**, 3313–3325.

Price J. R. and Velbel M. A. (2003) Chemical weathering indices applied to weathering profiles developed on heterogeneous felsic metamorphic parent rocks. *Chem. Geol.* **202**, 397–416.

Price J. R., Velbel M. A. and Patino L. C. (2005) Allanite and epidote weathering at the Coweeta Hydrologic Laboratory, western North Carolina, USA. *Am. Mineral.* **90**, 101–114.

Rosso J. J. and Rimstidt J. D. (2000) A high resolution study of forsterite dissolution rates. *Geochim. Cosmochim. Acta* **64**, 797–811.

Ryan J. G., Yurkovich S., Peterson V., Burr J. and Kruse S. (2005) Geology and petrogenesis of mafic and ultramafic rocks of the Willets-Addie area, central Blue Ridge, NC. In *Blue Ridge Geology Geotraverse East of the Great Smoky Mountains National Park Western North Carolina* (eds. R. D. Hatcher Jr. and A. J. Merschat). Carolina Geological Society Annual Field Trip Guidebook, pp. 91–98.

Santelli C. M., Welch S. A., Westrich H. R. and Banfield J. F. (2001) The effect of Fe-oxidizing bacteria on Fe–silicate mineral dissolution. *Chem. Geol.* **180**, 99–115.

Schott J. and Berner R. A. (1985) Dissolution mechanisms of pyroxenes and olivines during weathering. In *The Chemistry of Weathering* (ed. J. I. Drever). Reidel, Dordrecht, The Netherlands, pp. 35–53.

Schulte M., Blake D., Hoehler T. and McCollom T. (2006) Serpentinization and its implications for life on early Earth and Mars. *Astrobiology* **6**, 364–376.

Seyama H., Soma M. and Tanaka A. (1996) Surface characterization of acid-leached olivines by X-ray photoelectron spectroscopy. *Chem. Geol.* **129**, 209–216.

Smith K. L., Milnes A. R. and Eggleton R. A. (1987) Weathering of basalt: formation of iddingsite. *Clay Clay Mineral.* **35**, 418–428.

Swanson S. E., Raymond L. A., Warner R. D., Ryan J. G., Yurkovich S. P. and Peterson V. L. (2005) Petrotectonics of mafic and ultramafic rocks in Blue Ridge terranes of western North Carolina and northern Georgia. In *Blue Ridge Geology Geotraverse East of the Great Smoky Mountains National Park Western North Carolina* (eds. R. D. Hatcher Jr. and A. J. Merschat). Carolina Geological Society Annual Field Trip Guidebook, pp. 73–90.

Velbel M. A. (1983) A dissolution–reprecipitation mechanism for the pseudomorphous replacement of plagioclase feldspars by clay minerals during weathering. In *Pétrologie des Altérations et des Sols, Volume I*, vol. 71 (eds. D. Nahon and Y. Noack). *Sciences Géologiques, Mémoires (Strasbourg)*, pp. 139–147.

Velbel M. A. (1984) Natural weathering mechanisms of almandine garnet. *Geology* **12**, 631–634.

Velbel M. A. (1986) Influence of surface area, surface characteristics, and solution composition on feldspar weathering rates. In *Geochemical Processes at Mineral Surfaces*, vol. 323 (eds. J. A. Davis and K. F. Hayes). American Chemical Society, Symposium Series, pp. 615–634.

Velbel M. A. (1993) Formation of protective surface layers during silicate-mineral weathering under well-leached, oxidizing conditions. *Am. Mineral.* **78**, 408–417.

Velbel M. A. (1999) Bond strength and the relative weathering rates of simple orthosilicates. *Am. J. Sci.* **299**, 679–696.

Velbel M. A. (2004) Laboratory and homework exercises in the geochemical kinetics of mineral-water reaction: rate law, Arrhenius activation energy, and the rate-determining step in the dissolution of halite. *J. Geosci. Educ.* **52**, 52–59.

Velbel M. A. (2007) Surface textures and dissolution processes of heavy minerals in the sedimentary cycle: examples from pyroxenes and amphiboles. In *Heavy Minerals in Use*, vol. 58 (eds. M. Mange and D. Wright). *Dev. Sed.*, pp. 113–150.

Velbel M. A. and Ranck J. M. (2008) Etch pits on naturally altered olivine from dunites of the Appalachian Blue Ridge Mountains, North Carolina, USA. *Mineral. Mag.* **72**, 149–152.

Velbel M. A., Basso, Jr., C. L. and Zieg M. J. (1996) The natural weathering of staurolite: crystal-surface textures, relative stability, and the rate-determining step. *Am. J. Sci.* **296**, 453–472.

Velbel M. A., McGuire J. T. and Madden A. S. (2007) Scanning electron microscopy of garnet from southern Michigan soils: etching rates and inheritance of pre-glacial and pre-pedogenic grain-surface textures. In *Heavy Minerals in Use*, vol. 58 (eds. M. Mange and D. Wright). *Dev. Sed.*, pp. 413–432.

Wegner M. W. and Christie J. M. (1974) Preferential chemical etching of terrestrial and lunar olivines. *Contrib. Mineral. Petrol.* **43**, 195–212.

Wegner M. W. and Christie J. M. (1976) Chemical etching of dislocations in forsterite. *Contrib. Mineral. Petrol.* **59**, 131–140.

Welch S. A. and Banfield J. F. (2002) Modification of olivine surface morphology and reactivity by microbial activity during chemical weathering. *Geochim. Cosmochim. Acta* **66**, 213–221.

Wicks F. J. and Whittaker E. J. W. (1977) Serpentine textures and serpentinization. *Can. Mineral.* **15**, 459–488.

Wilshire H. G. (1958) Alteration of olivine and orthopyroxene in basic lavas and shallow intrusions. *Am. Mineral.* **43**, 120–147.

Wilson M. J. (1975) Chemical weathering of some primary rock-forming minerals. *Soil Sci.* **119**, 349–355.

Wilson M. J. (2004) Weathering of the primary rock-forming minerals; processes, products and rates. *Clay Mineral.* **39**, 233–266.

Wilson M. J. and Jones D. (1983) Lichen weathering of minerals: implications for pedogenesis. In *Residual Deposits: Surface Related Weathering Processes and Materials*, vol. 11 (ed. R. C. L. Wilson). Geological Society Special Publication, pp. 5–12.

Wogelius R. A. and Walther J. V. (1992) Olivine dissolution kinetics at near-surface conditions. *Chem. Geol.* **97**, 101–112.

Young, III, C. (1969) Dislocations in the deformation of olivine. *Am. J. Sci.* **267**, 841–852.

Associate editor: Jacques Schott